Design of a Hybrid Positioner-Fixture for Six-axis Nanopositioning and Precision Fixturing

Mangudi Varadarajan Kartik and Martin L. Culpepper*
MIT Department of Mechanical Engineering
77 Massachusetts Avenue; Cambridge, MA 02139

This paper introduces a moving groove fixture which can be operated in two modes; as (1) a nanometer-level repeatable exact constraint fixture or (2) as a high load capacity, six-axis nanopositioner. Actuators, sensors and flexures are integrated into the structural loop of the fixture, thereby enabling controlled changes in fixture geometry to be used for nanometer/micro-radian-level positioning. Models of fixture kinematics and fixture stiffness were generated and used to design a proof-of-concept prototype. When operated in fixture mode, experiments show standard deviation in point-to-point repeatability of 11, 11, and 40 nm in x, y, and z; and 0.7, 0.3, and 0.3 micro-radians in θx, θy and θz. When operated in Nanopositioner mode, the device demonstrated 4nm resolution and a range of 40x40x80 microns in translation and 800x800x400 micro-radians in rotation. The fixture possesses a load capacity of 450 N, a measured stiffness of 10 N/micron and a measured natural frequency of 200 Hz. The combination of a positioner and a fixture characteristics enables one to adjust the fixtured position of a device (improve fixture accuracy) and then repeatably fixture about that position and orientation.

Keywords: Accuracy, repeatability, fixture, palletized, kinematic coupling, exact constraint, nanopositioner, nanomanufacturing, compliant mechanism, flexure, six axis

---

1. Introduction

1.1. Characteristics of fixtures and positioning devices

Alignment and positioning equipment are important as they are required in nearly all research and manufacturing processes. The increasing focus on nano-scale engineering has forced engineers and scientists to think about the types of alignment devices which will be required for new and emerging applications. At present, they may choose from two types of state-of-the-art devices; either fixtures or positioners. Fixtures are devices which define a part's fixated orientation and location via a fixed, geometry. Positioners are devices which define variable position and orientation via an adjustable geometry. Table 1 provides a comparison of the common performance for each type of device. The numbers for the device with better performance are listed in italics.

Table 1: The order of magnitude of precision fixture and positioner performance characteristics

	Fixture	Positioner	Ratio
Accuracy [nm]	10 000s	*10s*	10^3
Repeatability [nm]	100s	*10s*	10^1
Load capacity [N]	*1000s*	10s	10^2
Stiffness [N/micron]	*10s*	1s	10^1
Natural Frequency [Hz]	*100s*	10s	10^1
Cost [$]	*100s*	10 000s	10^{-2}

The following paragraphs briefly describe the reason for the difference in performance.

Precision fixtures have been capable of achieving sub-micron repeatability for some time. However, the positioning accuracy of these fixtures is closely linked to manufacturing and assembly errors. As such, passive fixtures such as kinematic couplings achieve practical accuracy of 10 microns [01, 02] at best. In

---

*Phone: 617 452 2395; Fax: 617 812 0384; E-mail: culpepper@mit.edu

contrast, the active adjustment capability of positioners enables them to achieve tens of nanometers accuracy and repeatability.

The structure of passive fixtures is not constrained by the need to change geometry; therefore they may be designed with emphasis on high load capacity. The geometry of positioners must be variable and so their structures require bearings and joints which are orders of magnitude less stiff than the continuous structure of a fixture. High stiffness is importance as it improves the disturbance rejection capabilities of a machine. For instance, errors caused by external forces and vibrations generally decrease as stiffness increases.

The improved stiffness characteristics of fixtures are in-part responsible for their higher natural frequencies. In contrast, positioners have lower natural frequencies because they include the additional weight of actuation components and they often incorporate high-performance, low-stiffness joints or bearings. In the end, the cost of active elements, precision bearings and the need for precision assembly of mechanisms-actuators-bearings make the cost of positioners higher than those of passive fixtures.

The preceding discussion demonstrates the difficulties which must be overcome to make either device have the desirable characteristics of both devices. This begs the question, "Might we be able to somehow combine the concepts of the fixture and positioner in a way which enables us to obtain the good characteristics of each device and none of the bad?

1.2. Conceptual approaches to integrating fixture and positioner technology

One might attempt to synthesize a design in which the functional and physical characteristics of the fixture and positioner devices remain separated and the devices are then added in series or parallel. From a positioning perspective, it would be sufficient to put the two devices in series (e.g. integrate a precision interface within the stage of a positioner). A part could be roughly aligned using the fixture and then accurately oriented and positioned using the positioner. Unfortunately, in this serial configuration the fixture and positioner would experience the same loading. As such, the cost, stiffness, load capacity and dynamic characteristics of this concept would at best approach those of the positioner. On the other hand, the parallel addition of a fixture and positioner is inappropriate as this would yield an over constrained design containing redundant kinematic chains.

A different conceptual approach is required. Toward this end, we have developed a conceptual model and supporting parametric models for a hybrid positioner-fixture (HPFs). The HPF incorporates precision flexure bearings, exact constraint elements and actuators/sensors. The combination of these elements enables the HPF to achieve passive repeatability of tens of nanometers and active correction of alignment errors over a range of tens of microns and hundreds of micro-radians. The key in this approach is to use the capability of flexures to possess high stiffness in ζ directions/orientations and low stiffness in 6- ζ directions/orientations. This allows us to use flexures to simultaneously provide position adjustment in 6- ζ directions and constraint in ζ directions. In this work, the flexure bearings are incorporated into the structural loop of the HPF such that they enable:

(1) Positioning: The flexure bearing's directions of high compliance are arranged parallel to the directions in which we wish to actuate. These directions are laid out so that they do not have a detrimental effect on the HPF stiffness when a high-stiffness actuator is used in parallel with the flexure.

(2) Fixturing: The flexure bearing's directions of high stiffness and high load capacity are aligned with the vectors of force transmittal through the fixture's structural loop, thereby enabling high load capacity and stiffness.

1.3. Contents of this paper

In this paper, we describe the conceptual modeling of HPFs and how they may be parametrically modeled. Experimental results are used to demonstrate the accuracy of the parametric models, the capability of the HPF to act as a six-axis positioning device (six-axis displacements), and its capability to act as a positioner (accuracy and repeatability).

2. Linking the characteristics and performance of fixtures and positioners

2.1. Analogy between constraints in fixtures and positioning mechanisms

The fundamental difference between fixtures and positioners is their respective static and variable geometric/kinematic characteristics. Fixtures ideally have static structures while the structure of positioners is comprised of geometrically variable mechanisms. Any attempt to acquire the desirable characteristics of both devices must start with an effort to link the characteristics of a fixture's structure and a positioner's mechanisms. For small motions, it can be shown that exact constraint fixtures are kinematically equivalent to parallel mechanisms [01]. For example, the right side of Fig. 1 shows how the 6 ball-groove constraints (2 per ball groove joint x 3 grooves) form the same arrangement of constraints that exist in a Stewart-Gough platform.

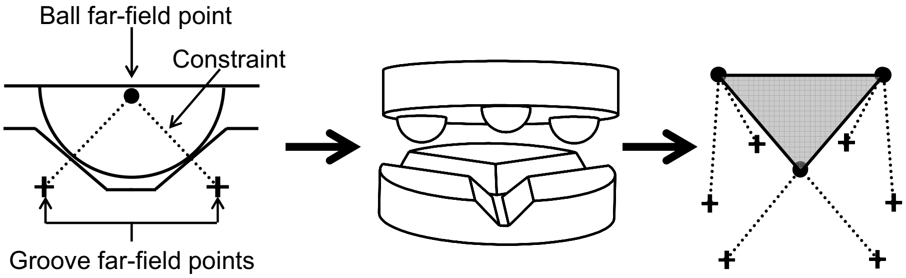

Figure 1: Analogy between the constraints of a kinematic coupling and the constraints of a Stewart-Gough platform

From this analogy we may equate the changing of fixture constraints with the actuation of a 6 axis mechanism. Therefore, if the position of the balls and/or groove may be controlled with respect to the components to which they are attached, we may affect changes in position and orientation between the fixtured components.

2.2. HPF concept

Although examples of two [03] and three [04] axes corrective fixtures exist, we must be able to align in six axes in order to (1) achieve any combination of position-orientation and (2) to correct parasitic alignment errors. The only existing, 6 axis adjustable coupling, an eccentric ball-shaft design shown on the right side of Fig. 2, is limited to micron-level repeatability and accuracy [01] as a consequence of needing rolling element bearings.

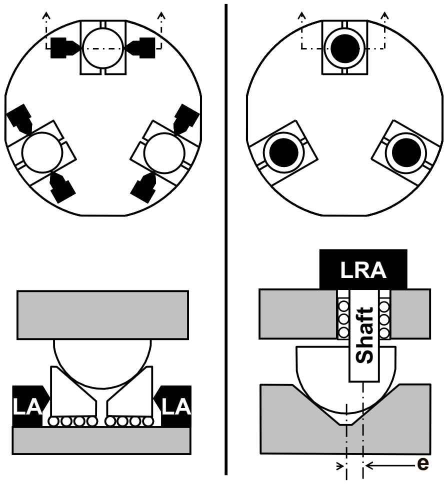

Figure 2: Moving groove (left) and eccentric ball (right) HPF designs. LA = linear actuator and LRA = linear-rotary actuator

In this paper, we investigate an alternate six-axis design in which the balls are rigidly attached to their respective component while the groove surfaces are actively positioned. This arrangement is shown on the left side of Fig. 2. In this design, the groove surfaces are mounted to bearings which guide them parallel to the plane of coupling and perpendicular to the groove's plane of symmetry. At each ball-groove joint, the in-plane and out-of-plane displacements of the ball-equipped (top) component with respect to the groove-equipped component may be achieved as shown in Fig. 3.

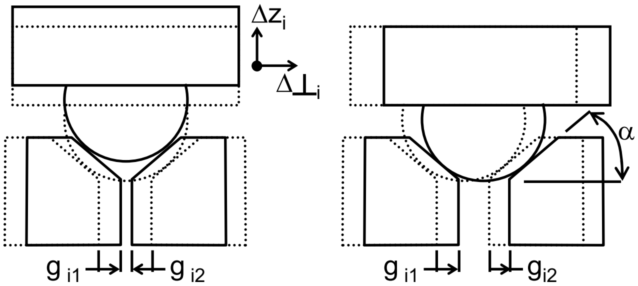

Figure 3: Groove displacements which induce out-of-plane (left) and in-plane (right) displacements of the top component

Each i^{th} ball-groove joint is therefore capable of two independent position inputs, g_{i1} and g_{i2}. If the grooves are laid out to ensure linear independence of the groove constraints, the device will have six independent position inputs. When these inputs are changed for each joint, it becomes possible to control the position and orientation of the ball-equipped component in six DOF.

3. Kinematic modeling

In this section, we discuss the approach used to model the positioning kinematics of the HPF.

3.1. Relationship between actuator displacement and ball displacement

In this analysis, we treat the grooved component as grounded and the ball-equipped component as mobile. The change in position of the balled-component's coupling centroid is defined by the changes in position of the ball centers. Equations 1 and 2 describe the relationship between ball displacement and groove displacement for ball i.

$$\Delta \perp_i = \frac{g_{i1} - g_{i2}}{2} \qquad (1)$$

and,

$$\Delta z_i = \left(\frac{g_{i1} + g_{i2}}{2} \right) . \tan \alpha \qquad (2)$$

Subscripts 1 and 2 represent the leftmost and rightmost groove surfaces as seen looking down a vector which lies in the groove's plane of symmetry and which intersects the ball's center and the coupling centroid. Displacement of the grooves toward the center of the ball is assigned positive as this corresponds to positive displacement of the actuators.

3.2. Relationship between ball center displacements and fixture in-plane displacements

Vector-based approaches to fixture design are widely used in robotics, reconfigurable fixture systems and machine structure design. In precision applications, this approach has been applied to model the micron-level displacements and errors in static kinematic fixtures [02], kinematic fixtures with two-axis adjustability [03] and six-axis exact constraint fixtures [01]. Here, we use a vector-based approach which uses the projection of vector loops on the homed plane of coupling to model in-plane fixture displacements. This approach is unique in that it enables direct calculation of the forward and inverse kinematic relationships between motion and actuator input. Three vector loops, one for each ball, are constructed as shown in Fig. 4. In this model, the magnitude of vector | $\boldsymbol{r}_{ib\perp}$ |= $\Delta\perp_i$, is given by Eqxn. 1. This vector is always perpendicular to the corresponding groove's plane of symmetry.

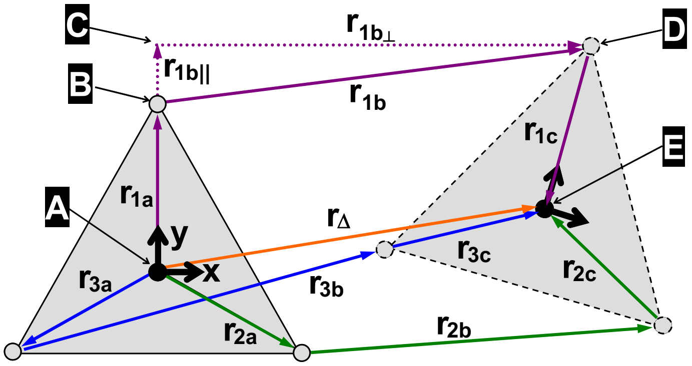

Figure 4: In-plane vector loops of the HPF model. Note, each ball-groove joint is pierced by one vector loop

In Fig. 4, each i^{th} loop consists of several vectors which trace a path from the home position of the ball-equipped component's coupling centroid (point A) to its displaced coupling centroid (point E). The vector loops are run through each ball-grove joint. Vectors are differentiated by subscripts *ij*, where *i* corresponds to the ball-grove joint number and *j* corresponds to the vector number. A system of equations, represented by Eqxn. 3, may be used to describe the fixture's in-plane position, ΔXc, ΔYc, and orientation, $\Delta\theta z_c$.

$$\vec{r}_{ia} + \vec{r}_{ib\|} + \vec{r}_{ib\perp} + \vec{r}_{ic} = \vec{r}_\Delta \qquad (3)$$

Fig. 5 contains an overlay of the vector loop for ball-groove joint 1 and the ball-grooves of a kinematic coupling. Points A – E in Fig. 5 correspond to points A – E in Fig. 4.

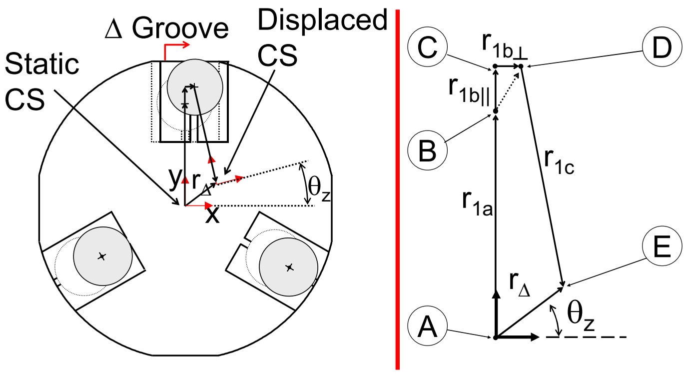

Figure 5: Detailed view of in-plane kinematic model in relationship to kinematic coupling geometry (top component removed for clarity). Note the static coordinate system (CS) and displaced CS. The coordinate systems lie at the coupling centroid as calculated from the layout of the ball positions when all $r_{ib\perp} = 0$.

For each loop *i*, Eqxn. 3 represents the two relationships shown in Eqxns. 4 and 5.

$$L_{ia}\cdot\cos(\theta_{ia})+L_{ib||}\cdot\cos(\theta_{ia})+L_{ib\perp}\cdot\sin(\theta_{ia})+L_{ic}\cdot\cos(\theta_{ic})=\Delta X_c \tag{4}$$

$$L_{ia}\cdot\sin(\theta_{ia})+L_{ib||}\cdot\sin(\theta_{ia})-L_{ib\perp}\cdot\cos(\theta_{ia})+L_{ic}\cdot\sin(\theta_{ic})=\Delta Y_c \tag{5}$$

The variables L_{ij} represent the length of vector r_{ij}. In this model θ_{ic} and $\Delta\theta_z$ are linked by Eqxn. 6, and L_{ia} is equal to L_{ic}.

$$\theta_{ic}=\theta_{ia}+\pi+\Delta\theta z \tag{6}$$

When Eqxn. 6 is substituted into Eqxns. 4 and 5, L_{ic} is substituted for L_{ia}, and we assume small angle approximations ($\sin(\Delta\theta z_c)\sim(\Delta\theta z_c)$ and $\cos(\Delta\theta z_c)\sim 1$), we obtain the matrix equation provided in Eqxn. 7.

$$\begin{bmatrix} 1 & 0 & -L_{1c}\cdot\sin(\theta_{1a}) & -\cos(\theta_{1a}) & 0 & 0 \\ 0 & -1 & -L_{1c}\cdot\cos(\theta_{1a}) & \sin(\theta_{1a}) & 0 & 0 \\ 1 & 0 & -L_{2c}\cdot\sin(\theta_{2a}) & 0 & -\cos(\theta_{2a}) & 0 \\ 0 & -1 & -L_{2c}\cdot\cos(\theta_{2a}) & 0 & \sin(\theta_{2a}) & 0 \\ 1 & 0 & -L_{3c}\cdot\sin(\theta_{3a}) & 0 & 0 & -\cos(\theta_{3a}) \\ 0 & -1 & -L_{3c}\cdot\cos(\theta_{3a}) & 0 & 0 & \sin(\theta_{3a}) \end{bmatrix}\cdot\begin{bmatrix} \Delta X_c \\ \Delta Y_c \\ \Delta\theta z_c \\ L_{1b||} \\ L_{2b||} \\ L_{3b||} \end{bmatrix}=\begin{bmatrix} L_{1b\perp}\cdot\sin(\theta_{1a}) \\ L_{1b\perp}\cdot\cos(\theta_{1a}) \\ L_{2b\perp}\cdot\sin(\theta_{2a}) \\ L_{2b\perp}\cdot\cos(\theta_{2a}) \\ L_{3b\perp}\cdot\sin(\theta_{3a}) \\ L_{3b\perp}\cdot\cos(\theta_{3a}) \end{bmatrix} \tag{7}$$

Small angle approximations are appropriate as the second order effects on position due to angle coupling result in errors on the order of 10^{-3} – 10^{-6} smaller than the displacements of interest. The right side of Eqxn. 7 consists of the actuation inputs, $L_{ib\perp}$, and geometry variables. This kinematic relationship is different from previous approaches in that it enables the immediate calculation of forward and reverse kinematic solutions without iteration.

3.3. Relationship between ball center displacements and the fixture's out-of-plane displacements

The out-of-plane displacement, ΔZ_c, and rotations, $\Delta\theta x_c$ and $\Delta\theta y_c$, are captured using translations of the ball centers perpendicular to part containing the grooves [01]. Figure 6 shows the planes formed by the homed and displaced position of the ball centers. The motion of each ball relative to the homed plate is given by Eqxn. 2 as Δz_i.

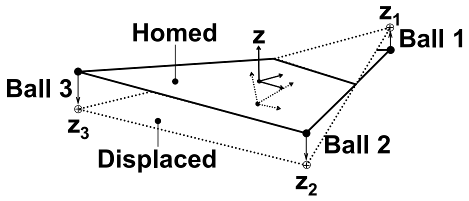

Figure 6: Out-of-plane vector model of HPF

Given the location of each ball center, one may form an equation for the plane containing the ball centers and then solve for (1) the location of the coupling centroid in z and (2) the orientation of the plane as described by its normal vector. Changes in position and normal vector due to the out-of-plane ball displacements, Δz_i, are used to determine the change in ΔZ_c, $\Delta\theta x_c$ and $\Delta\theta y_c$ [01] The relationships between ball displacements and fixture displacements are provided in Eqxn. 8 – 10 [01]. The abbreviations s[θ] = sin[θ] and c[θ] = cos[θ] have been used in Eqxns 8 – 10.

$$\Delta\theta x_c = -\left(\frac{L_1.(s[\theta_1].\theta_z - c[\theta_1]).(\Delta z_2 - \Delta z_3) + L_2.(s[\theta_2].\theta_z - c[\theta_2]).(\Delta z_3 - \Delta z_1) + L_3.(s[\theta_3].\theta_z - c[\theta_3]).(\Delta z_1 - \Delta z_2)}{L_1.L_2.s[\theta_2 - \theta_1] + L_2.L_3.s[\theta_3 - \theta_2] + L_3.L_1.s[\theta_1 - \theta_3]}\right) \tag{8}$$

$$\Delta\theta y_c \approx \left(\frac{L_1.(s[\theta_1] + c[\theta_1].\theta_z).(\Delta z_2 - \Delta z_3) + L_2.(s[\theta_2] + c[\theta_2].\theta_z).(\Delta z_3 - \Delta z_1) + L_3.(s[\theta_3] + c[\theta_3].\theta_z).(\Delta z_1 - \Delta z_2)}{L_1.L_2.s[\theta_2 - \theta_1] + L_2.L_3.s[\theta_3 - \theta_2] + L_3.L_1.s[\theta_1 - \theta_3]}\right) \tag{9}$$

$$\Delta Z_c \approx L_1(\theta y_c.c[\theta_1] - \theta x_c.s[\theta_1]) + \Delta z_1 \tag{10}$$

3.4. Implementation of kinematic theory in a spreadsheet model

Equations 7 – 10 may be used to provide forward and inverse kinematic solutions for six axis motions. The theory was incorporated into an Excel spreadsheet (available for download at psdam.mit.edu/tools/index.html) which solves the forward and reverse kinematics of a moving groove HPF. The accuracy of the kinematic model was checked by comparing simulated displacements with displacements measured from a solid model of the HPF. The difference between predicted and measured results was less than 5 nanometers/1 μradians in each of the following scenarios:

(1) The planar displacement ΔX_c, ΔY_c and $\Delta\theta z_c$ examples portrayed in X

(2) The non-planar displacements, $\Delta\theta x_c$, $\Delta\theta y_c$ and ΔZ_c

(3) Various combinations of planar and non-planar displacements

4. Stiffness modeling approach

In this section we provide a brief overview of how the stiffness of the compliant components are modeled and then combined to form a model for the stiffness of the HPF.

4.1. Ball-groove contacts

The ball-groove contacts are modeled as non-linear springs with stiffness and deflection characteristics governed by Hertzian contact mechanics [05, 06]. The normal and tangential stiffness of the contacts is given by Eqxns. 11 and 12 respectively.

$$k_n = \left[6 \cdot F_n \cdot R_e \cdot (E_e)^2\right]^{1/3} \tag{11}$$

$$k_t = 8 \cdot r \cdot G_c \cdot \left[1 - \frac{F_t}{\mu \cdot F_n}\right]^{1/3} \tag{12}$$

Where F_t is the tangential force, F_n is the normal contact force, the equivalent radius, R_e, is given by Eqxn. 13, the contact patch radius, r, is given by Eqxn 14, and the equivalent modulus, E_e, is given by Eqxn. 15.

$$R_e = \left(\frac{1}{R_{ball}} + \frac{1}{R_{groove}}\right)^{-1} \tag{13}$$

$$r = \left[\frac{3}{4} \cdot \frac{R_e}{E_e} \cdot F_n\right]^{\frac{1}{3}} \tag{14}$$

$$E_e = \left(\frac{1-\nu_{ball}}{E_{ball}} + \frac{1-\nu_{groove}}{E_{groove}}\right)^{-1} \tag{15}$$

It should be noted that the stiffness of the contact is dependant upon load, therefore stiffness properties of the fixture will be dependant upon the magnitude of the nesting preload.

4.2. Groove flexure bearings

The need for groove flexure bearings

Why are the groove flexure bearings required? It is important to note that the pattern of grooves and balls must remain geometrically compatible throughout any actuation. This fact, in combination with the change we are making to the groove pattern combine to yield the desired displacement of the HPF. In essence, we change the pattern and the coupling attempts to adjust position to maintain geometric compatibility. A consequence of the position adjustment is that the balls must slide along the grooves. The sliding motions are illustrated in Fig. 7. In the figure, the leftmost diagram shows the balls and groove of the coupling. As the top groove is actuated to the left, (noted by motion 1), the bottom balls must move along their grooves (noted by motions 2) to maintain geometric compatibility between the ball-groove patterns.

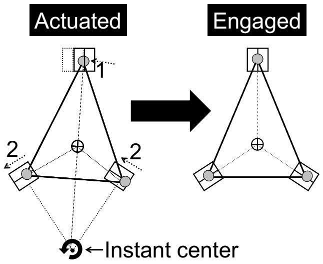

Figure 7: Ball-groove sliding “2” due to actuation motion “1”

As a result, it is typical to obtain the wear marks shown in Fig. 8. The wear marks along the groove are noted as "2" in keeping with the sliding descriptions in Fig. 7.

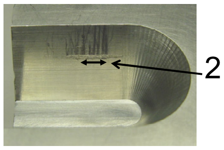

Figure 8: Wear of groove interface due to sliding contact, "*2*" indicates wear from ball sliding along groove

This wear is not desired as it imparts non-predictable, time varying changes in the kinematic loop (the contact between the balls and grooves) of the device. This wear, imparts position uncertainties in fixture performance which are on the same order of the wear errors.

Groove flexure concepts

The first step in developing a conceptual model which solves this problem is to understand the minimum function of the groove surface. From Fig. 1, we can see that the groove is only required to offer high stiffness and load carrying capacity normal to the groove surface. To reduce over constraint, the stiffness of the ball-groove contact perpendicular to the normal direction should be as small as possible. This can be accomplished by using a bearing whose stiffness is aligned with the normal contact vector. The general bearing requirements are as follows:

(1) Bearing range parallel to the groove surface of at least the positioning range of the HPF

(2) High normal stiffness, preferably at some factor 10 higher than the ball-flat Hertzian contact stiffness.

(3) Stiffness parallel to the groove surface which is at least 10 times lower than the preloaded ball-groove tangential stiffness. The (a) minimizes the deformation and therefore stress at the ball-groove contact and (b) ensures that no sliding occurs between the ball and groove.

(4) Hysteresis at some desired factor lower than desired positioning resolution

Specific requirements for many precision applications include:

(5) Vacuum compatible

(6) No supporting equipment costs (e.g. electronics or fluid systems)

Flexure bearings are one of the few types of bearings which are capable of satisfying all of the preceding requirements. They have been used in exact constraint devices to minimize friction hysteresis effects at non-sliding contacts [07], to prevent over constraint in ball-cone fixtures [06, 08] and to enable high-stiffness and sealed contact [09].

The question now becomes what type of flexure bearings should be used. The bearing must be capable of high stiffness in one direction and relatively low stiffness in perpendicular directions. Although one may use the axisymmetric hour glass type of flexures shown in Fig. 9, the kinematics of these flexures leads them to travel in an arc, thereby imparting parasitic errors to the kinematics of the fixture. It is better to have a flexure which exhibits no inherent parasitic errors.

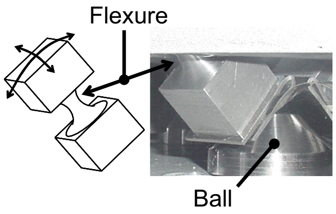

Figure 9: Prototype of hour glass groove flexure bearing for HPF

The flexure bearing concept shown on the left of Fig. 10 is capable of high stiffness normal to the plane of the paper and relatively low stiffness parallel to the pane of the paper. In practice, a polished, hardened steel plate is bonded to the surface of the flexure. The plate surface forms the contacting surface for the corresponding ball. If we assume a sufficient preload is forcing the ball into contact with the plate surface, then any attempt by the ball to move along the groove (parallel to the plate surface) will cause the flexure beams to comply. The center span of the flexure and the groove plate will travel with the ball along the groove. As such, the ball and groove will not slide relative to each other [10].

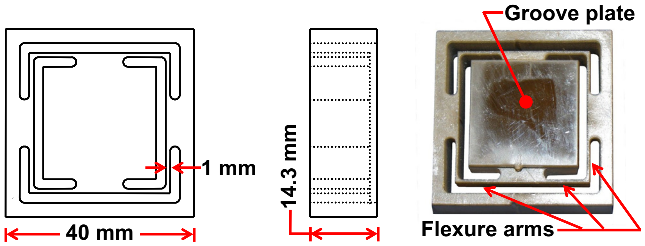

Figure 10: Prototype of planar groove flexure bearing for HPF

Groove flexure modeling

The approach used to model the compliant elements of the fixture is summarized in Fig. 11. The general approach will be explained below in brief and then described with specific reference to the groove flexure bearing.

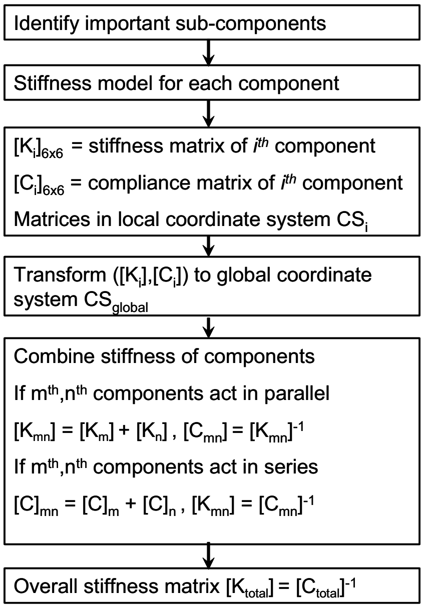

Figure 11: Direct stiffness approach to modeling systems of rigid and compliant parts

A stiffness matrix and compliance matrix are obtained via the direct stiffness approach as explained by Hale [11]. The stiffness of each compliant element of a flexure is assigned to a local (local to the element) coordinate system and then transformed into the local coordinate system of the flexure. The contributions of each beam's stiffness characteristics are then combined (according to parallel or serial arrangements) to form a stiffness matrix and a compliance matrix for the flexure. The stiffness characteristics of each compliant element (ball-groove contacts, guide flexures and groove flexures) will be transformed and combined to form a global stiffness matrix for the HPF.

The groove flexure is modeled as a combination of eight beams, as shown in Fig. 12. Each of the beam pairs 1-8, 2-3, 4-5 and 6-7 are in series, hence compliance of the pair equals the sum of individual compliances. This matrix relates the motion vector of the guided component at the groove flexure's local coordinate system, CS_{GF}, under the influence of the motion vector of external loads.

Figure 12: Model of planar groove flexure with showing local beam coordinates (left) and beam design parameters (right)

The compliance matrix for a single beam is given in Eqxn. 16. The columns in this matrix correspond to the rows of the load vector: $[F_x, F_y, F_z, M_x, M_y, M_z]^T$.

$$\mathbf{C}_{\mathbf{beam}} = \begin{bmatrix} \frac{1}{K_{xx}} & 0 & 0 & 0 & 0 & 0 \\ 0 & \frac{1}{K_{yy}} + \frac{a}{G \cdot w \cdot t} & 0 & 0 & 0 & \frac{-1}{K_{\theta zy}} \\ 0 & 0 & \frac{1}{K_{zz}} + \frac{a}{G \cdot w \cdot t} & 0 & \frac{-1}{K_{\theta yz}} & 0 \\ 0 & 0 & 0 & \frac{1}{K_{\theta xx}} & 0 & 0 \\ 0 & 0 & \frac{-1}{K_{z\theta y}} & 0 & \frac{1}{K_{\theta yy}} & 0 \\ 0 & \frac{1}{K_{y\theta z}} & 0 & 0 & 0 & \frac{1}{K_{\theta zz}} \end{bmatrix} \tag{16}$$

Where:

$$K_{xx} = \frac{E \cdot t \cdot w}{a} \tag{17}$$

$$K_{yy} = \frac{E \cdot w \cdot t^3}{4 \cdot a^3} \tag{18}$$

$$K_{zz} = \frac{E \cdot w^3 \cdot t}{4 \cdot a^3} \tag{19}$$

$$K_{y\theta z} = \frac{E \cdot w \cdot t^3}{6 \cdot a^2} \tag{20}$$

$$K_{\theta yz} = \frac{E \cdot w^3 \cdot t}{6 \cdot a^2} \tag{21}$$

$$K_{\theta zy} = \frac{E \cdot w \cdot t^3}{6 \cdot a^2} \tag{22}$$

$$K_{z\theta y} = \frac{E \cdot w^3 \cdot t}{6 \cdot a^2} \tag{23}$$

$$K_{\theta xx} = \frac{G \cdot w \cdot t^3}{16 \cdot a} \cdot \left[\frac{16}{3} - 3.36 \cdot \frac{t}{w} \cdot \left(1 - \frac{t^4}{12 \cdot w^4}\right)\right] \tag{24}$$

$$K_{\theta yy} = \frac{E \cdot w^3 \cdot t}{12 \cdot a} \tag{25}$$

$$K_{\theta zz} = \frac{E \cdot w \cdot t^3}{12 \cdot a} \tag{26}$$

and, t = thickness of beam, a = length of beam, w = width of beam, E = Young's modulus, and G = shear modulus. Through this parametric model, it is possible to optimize the stiffness properties, e.g. low in directions of desired motion and high in other directions/rotations, by tuning design the flexure's design parameters.

4.3. Guiding flexure bearing

The purpose of the guiding flexure is to ensure that the grooves are actuated with smooth motion and along a linear path. Figure 13 shows the conceptual model in which actuators are mounted into six sets of linear flexure bearings, e.g. guide flexure bearings, within a monolithic base. This design simplifies fabrication of the HPF as the base may be cut as a single piece via EDM or abrasive waterjet cutting. The geometry of the flexures may be biased such that they provide a preload on the actuator in the non-actuated state.

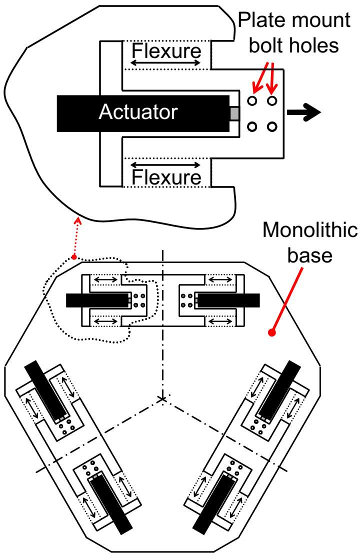

Figure 13: Top view of groove guide flexure bearings as machined within monolithic block

A model of the guided flexure bearing is shown in Fig. 14. For a guiding motion range, δz, of 50µm and beam thickness, t = 1 mm, $({}^{\delta z}/_{t})^2 = 0.0025 < 1$, therefore stress stiffening of the beams may be neglected and the beams may be modeled with linear stiffness properties. The steps used to model the stiffness of the flexure are identical to those covered for the groove flexure. Eqxns. 16 – 26 are also valid for modeling of the compliant elements in the guiding flexure. The direct stiffness method may again be used to form stiffness and compliance matrices for the guiding flexure as a whole. The model may then be used to ascertain the optimum size, shape, location and number of beams.

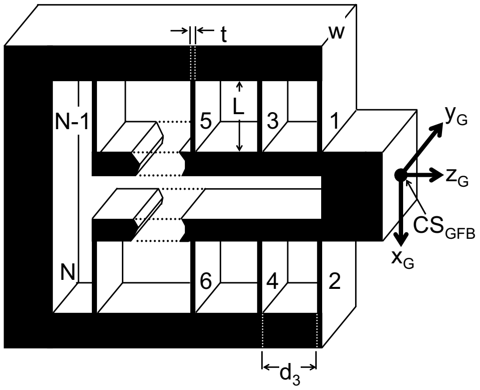

Figure 14: Model of grove guiding flexure bearing with N guiding beams

In designing this flexure we are interested in (1) setting the center of stiffness at the centroid of the guiding flexure beams and (2) ensuring that the line of action of the normal force, F_n, runs through this point. This is best understood via inspection of Fig. 15. By satisfying the two conditions, we minimize the amount of unwanted rotation the bearing will experience due to the moment caused by the contact force, F_n. The model of the groove guide flexure, shown in Fig. 15 was used to derive Eqxn. 27 which provides an expression for M_x as a function of design parameters.

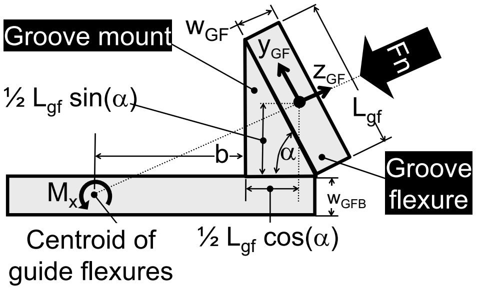

Figure 15: Center of stiffness model for the assembly of the guiding flexure bearing, groove mount, and groove flexure

$$M_x = F_n \cdot \sin(\alpha) \cdot \left(w_{GF} \cdot \cos(\alpha) + \frac{L_{GF} \cdot \sin(\alpha)}{2} + \frac{w_{GFB}}{2} \right) - F_n \cdot \cos(\alpha) \cdot \left(b + \frac{L_{GF} \cdot \cos(\alpha)}{2} + w_{GF} \cdot \sin\alpha \right) \tag{27}$$

The variable b is chosen such that $M_x = 0$, thereby reducing the vertical deflection of the guide flexure bearing when the groove contact is loaded. The appropriate value of b, for $\alpha = 60^\circ$ is shown in Eqxn. 28.

$$b_{Mx=0}\Big|_{\alpha=60^\circ} = \left[\frac{L_{GF} \cdot \left[\sin^2(\alpha) - \cos^2(\alpha)\right]}{2 \cdot \cos(\alpha)} + \frac{w_{GFB} \cdot \tan(\alpha)}{2} \right]_{\alpha=60^\circ} = \frac{L_{GFB}}{2} + \frac{\sqrt{3}}{2} \cdot w_{GFB} \tag{28}$$

4.4. System stiffness modeling

In modeling the stiffness of the HPF, we assume that the groove flexure bearing, the guiding flexure bearing and the ball-groove contacts comprise the major sources of compliant deformations. As such, they are modeled as compliant elements, e.g. springs, using the direct stiffness approach. The flexure bearings are modeled as linear compliant elements and the bal-groove joints are modeled as non-linear compliant Hertzian contacts. Each spring is assigned a local coordinate system. The compliance of the flexible parts (e.g. beams) within each element in the element's local coordinate system is transformed into reference frame of the element and the contributions of each flexible part are then combined to form a stiffness matrix for the element. The element's stiffness characteristics are then transformed into the HPF's coordinate system and then the contributions of each element are combined to form a stiffness matrix for the HPF. This matrix relates the motion of one coupled component (the ball-equipped component) with respect to the grounded (groove-equipped component) under the influence of external loads. This model was implemented in Matlab and used to predict the system stiffness as a function of fixture preload. The change in stiffness with preload (due to the non-linear ball-groove contact stiffness) may be seen in Table 2.

Table 2: Simulated HPF stiffness at coupling centroid – based on Matlab model

Preload	*Kxx* [N/µm]	*Kyy* [N/µm]	*Kzz* [N/µm]	*Kθxx* [kNm/rad]	*Kθyy* [kNm/rad]	*Kθzz* [kNm/rad]
450N	21.8	21.8	15.5	50.2	50.2	240.8
225N	20.4	20.4	14.6	47.3	47.3	223.0
45N	16.2	16.2	12.1	39.2	39.2	169.8

5. HPF design

The HPF kinematic and stiffness models were used to design a prototype moving groove HPF. The components of the prototype are shown in Fig. 16. The structural components and flexures are made from 6061 T6 Aluminum. The groove flexures are equipped with a hardened stainless steel plate, called a groove plate, which has been polished to a mirror finish. The plates are bonded to the dorsal surface of each groove flexure. The balls are comprised of hardened stainless steel which has been polished to mirror finish. The balls are bonded and pressed into brass collars which are in turn bonded and pressed into the top octagonal fixture plate. It is this plate which may be used to fixture and position other parts which are attached to it. The six guide flexures have been cut into a monolithic base component which is made from 6061 T6 Aluminum.

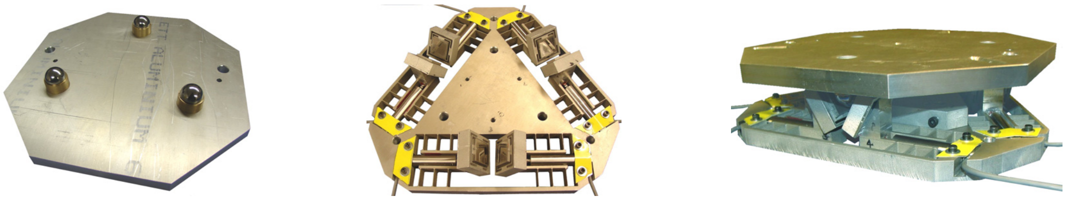

Figure 16: Prototype moving groove HPF, fixture envelope is 250mmx250mmx80mm

The cross section of the ball-grove joint shown in Fig. 17 illustrates how the grooves, groove flexures and groove plates are rigidly attached to the monolithic base which contains the guiding flexures. Piezo-electric actuators are integrated in the plane of the compliant mechanism such that they are structurally in parallel with their corresponding flexure bearing.

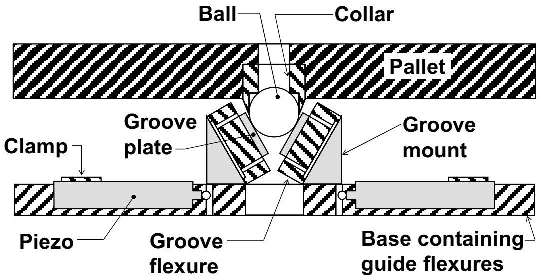

Figure 17: Cross section of a moving groove HPF ball-groove joint

Figure 18 provides an exploded view of the HPF in which the assembled relationship between the individual components is indicated by the parallel dotted lines.

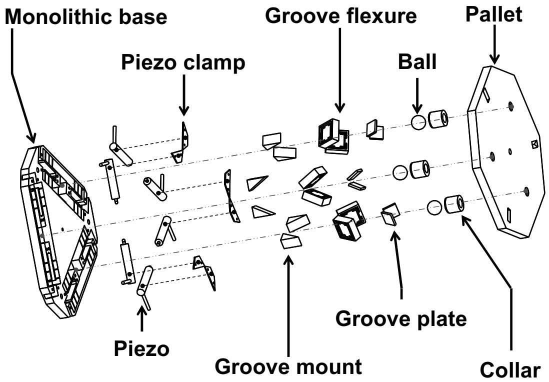

Figure 18: Exploded view of moving groove HPF

The models were used to design a HPF with the range characteristics shown in Table 3. The HPF was designed to possess a load capacity of 450 N and motion resolution of 4nm. Stiffness properties will be discussed in Section 6.6.

Table 3: Maximum design range of the moving groove HPF prototype

	X [µm]	Y [µm]	Z [µm]	θx [µradians]	θy [µradians]	θz [µradians]
Range	± 25	± 28	± 44	± 480	± 550	± 275

6. Experiment and discussion of results

Experiments were run in order to produce data which could be used to (1) ascertain the accuracy of the kinematic model, (2) understand how to calibrate the HPF, (3) verify that the groove flexures prevent relative sliding between the ball and groove, (4) characterize HPF repeatability in fixture mode, (5) ascertain the accuracy of the stiffness modeling and (6) understand the dynamic characteristics of the HPF. The following sub-sections provide summaries of these experiments and discuss the results which were obtained.

6.1. Experimental setup

Figure 19 shows the fixture mounted within an automated test rig. This test rig is equipped with an air piston which applies up to 450 N nesting preload. A flexure and a wobble pin between the fixture and piston were used to decouple off-axis preload forces which might be applied by the piston. A dSpace™ control system, cycles the air piston preload and either acquires readings from six capacitance probes or controls the six piezo actuators which position the grooves. High-pressure grease was used at the ball-groove interface to reduce settling time of the fixture. The setup was placed on an air table and allowed to come to thermal equilibrium within an insulated enclosure. The uncertainty in the measurement system varied for the type of test run, these numbers are reported separately for each test.

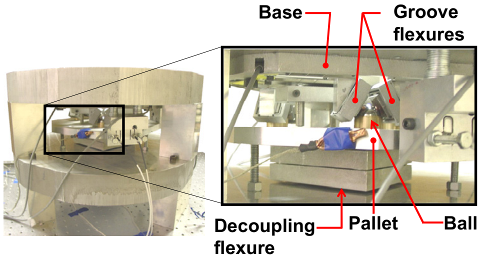

Figure 19: Test stand used to characterize HPF performance

6.2. Positioning: Open-loop performance in a non-calibrated state

Displacement tests were run to characterize the fixture's ability to provide pure displacement in each axis. The tests were run prior to calibration and without feedback control. Five positions were measured per test, one at the home position and two on either side of home. Between each position measurement, the preload was removed, the grooves were actuated to the desired position and then the preload was reapplied. The control/data acquisition was programmed to permit the fixture to settle for 30 seconds. Ten readings at each position were taken, and then averaged to obtain the final data point. The uncertainty of the measurements in this experiment was 60 nm. The displacements and parasitic errors measured in each test are provided in Fig. 20 and Fig. 21. The dotted line in the figures has a slope of unity and pierces the origin. If no errors are present between commanded and measured displacement, the data points should lie on this line.

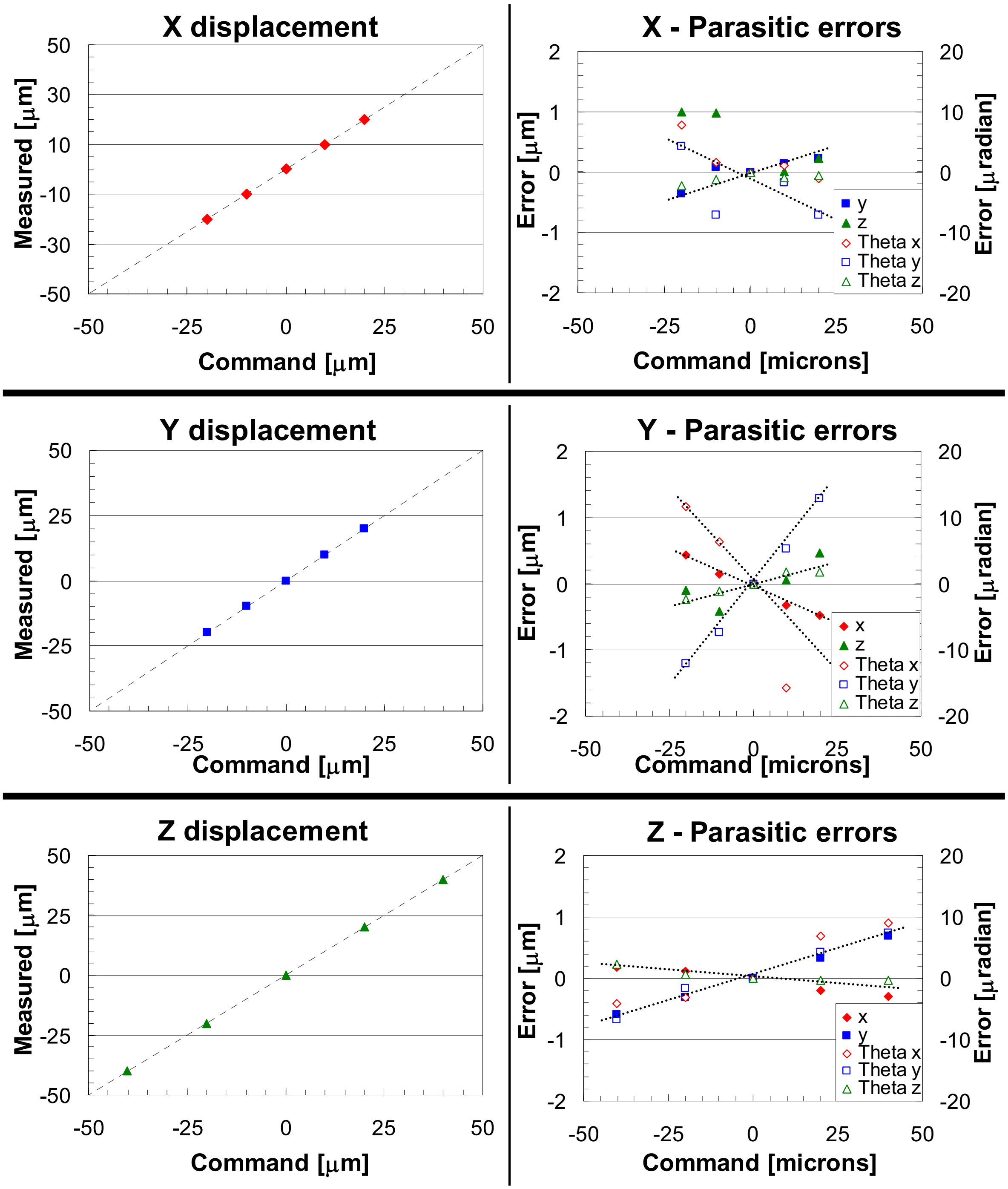

Figure 20: Translation tests results which compare the measured vs. commanded HPF behavior (left) and the parasitic errors as a function of commanded behavior (right)

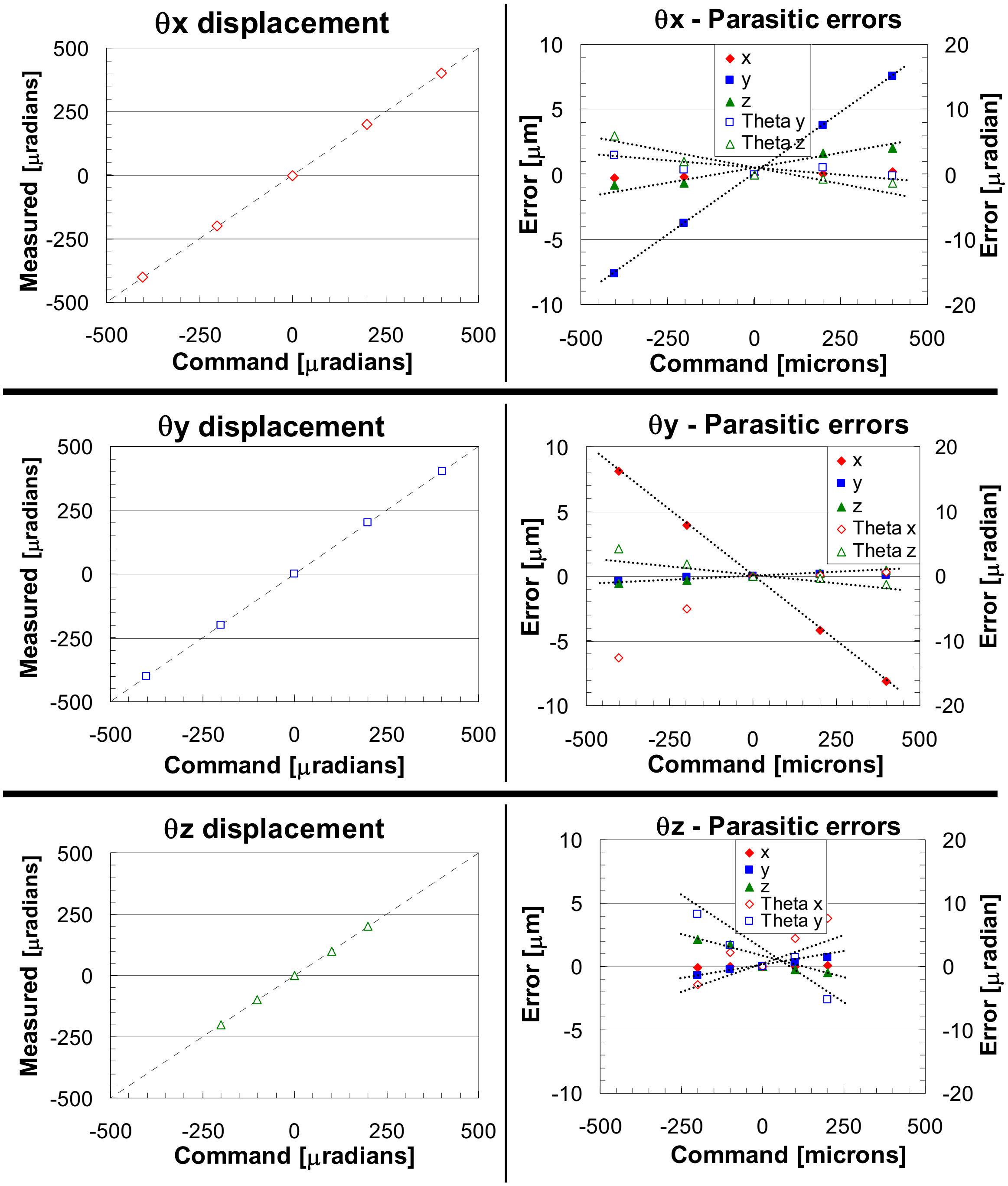

Figure 21: Orientation tests results which compare the measured vs. commanded HPF behavior (left) and the parasitic errors as a function of commanded behavior (right)

Several linear relationships between the commanded displacement and the parasitic errors may bee seen within the parasitic error plots. Some of these relationships are denoted on the right sides of Figs. 20 and 21 by line fits. The linear relationship between command and error is important as it shows these systematic errors are well-correlated to the actuation inputs. This opens the door to an elegant calibration technique which will be described later in this section. The systematic errors are in-part due to:

(1) Geometry errors: The physical components which define the HPFs kinematic chains differ from the ideal components which drive the kinematic model. For example there are errors in the reference and aligning features of each component which affect the assembly of each component. There are also errors in the size of the components which define the HPFs kinematic chains, repeatable parasitic errors in the guide flexures which are due to imperfect geometry of the compliant parts, and actuator misalignment errors.

(2) Material property errors: The model assumes isotropic material properties for Aluminum and a Young's Modulus of 30 ksi Young's Modulus. It is not uncommon for the modulus of Aluminum alloys which have been formed into sheet to differ by 5-10% fro the generic 30ksi value.

6.3. Removing systematic errors via calibration

The calibrated position and orientation vector, ***PO$_C$***, may be related to the model's predicted position and orientation vector, ***PO$_M$***, via the calibration matrix, ***C***, given in Eqxn. 29. In this approach, we are calibrating the HPF by modifying the model rather than modifying the hardware.

$$PO_C = C \cdot PO_M \rightarrow \left|\begin{matrix} \Delta Xc \\ \Delta Yc \\ \Delta Zc \\ \Delta\theta xc \\ \Delta\theta yc \\ \Delta\theta zc \end{matrix}\right|_{Calibrated} = \begin{bmatrix} C_{11} & C_{12} & C_{13} & C_{14} & C_{15} & C_{16} \\ C_{21} & C_{22} & C_{23} & C_{24} & C_{25} & C_{26} \\ C_{31} & C_{32} & C_{33} & C_{34} & C_{35} & C_{36} \\ C_{41} & C_{42} & C_{43} & C_{44} & C_{45} & C_{46} \\ C_{51} & C_{52} & C_{53} & C_{54} & C_{55} & C_{56} \\ C_{61} & C_{62} & C_{63} & C_{64} & C_{65} & C_{66} \end{bmatrix} \cdot \left|\begin{matrix} \Delta Xc \\ \Delta Yc \\ \Delta Zc \\ \Delta\theta xc \\ \Delta\theta yc \\ \Delta\theta zc \end{matrix}\right|_{Model} \qquad (29)$$

The rows of the matrix may be populated using the results of the single-axis tests. For instance, during an X axis move, ***PO$_M$***, would be $[\Delta Xc, 0, 0, 0, 0, 0]^T$ and the pre-calibrated, experimentally determined position and orientation vector, ***PO$_E$***, would be given by Eqxn 30.

$$\left|\begin{matrix} \Delta Xc \\ \Delta Yc \\ \Delta Zc \\ \Delta\theta xc \\ \Delta\theta yc \\ \Delta\theta zc \end{matrix}\right|_{Experimental}^{For\ PO_M = [\Delta Xc,0,0,0,0,0]^T} = \left|\begin{matrix} C_{11} \cdot \Delta Xc \\ C_{21} \cdot \Delta Xc \\ C_{31} \cdot \Delta Xc \\ C_{41} \cdot \Delta Xc \\ C_{51} \cdot \Delta Xc \\ C_{61} \cdot \Delta Xc \end{matrix}\right| \qquad (30)$$

The slope of the lines which were fitted to the data plotted in Figs. 20 and 21 may be used as the constants, ***C$_{i1}$***, for the first column of the calibration matrix. The same procedure may be used to populate the 2nd, 3rd, 4th, 5th, and 6th, columns using the ΔYc, ΔZc, $\Delta\theta xc$, $\Delta\theta yc$, and $\Delta\theta zc$ tests respectively. The completed matrix for the moving groove HPF prototype is provided in Eqxn. 31.

$$C = \begin{bmatrix} 0.998 & -0.023 & -0.006 & 0.001 & -0.020 & 0.000 \\ 0.013 & 1.000 & 0.016 & 0.019 & 0.001 & 0.003 \\ -0.025 & 0.016 & 1.000 & 0.004 & 0.001 & -0.007 \\ -0.184 & -0.950 & 0.182 & 1.002 & 0.016 & 0.023 \\ -0.174 & 0.623 & 0.171 & -0.003 & 1.002 & -0.029 \\ 0.036 & 0.110 & -0.031 & -0.009 & -0.007 & 1.002 \end{bmatrix} \qquad (31)$$

The improvement due to calibration will depend upon the quality of the line fit. Equation 32 shows the R^2 values for the calibration. The values $\boldsymbol{R_{ij}}$ correspond to the quality of the line fit for $\boldsymbol{C_{ij}}$.

$$R = \begin{bmatrix} 1.000 & 0.986 & 0.966 & 0.953 & 1.000 & 0.994 \\ 0.754 & 1.000 & 0.998 & 1.000 & 0.784 & 0.993 \\ 0.614 & 0.639 & 1.000 & 0.929 & 0.997 & 0.876 \\ 0.705 & 0.963 & 0.940 & 1.000 & 0.785 & 0.835 \\ 0.318 & 0.994 & 0.983 & 0.578 & 1.000 & 0.862 \\ 0.451 & 0.950 & 0.798 & 0.858 & 0.919 & 1.000 \end{bmatrix} \qquad (32)$$

The errors in the HPF prototype post calibration are listed in Table 4. The first data set indicates how well the HPF positions for a commanded single-axis move. The second set looks at the parasitic errors for all commanded displacements. In both sets, the numbers in the row labeled "Maximum" are the maximums of the absolute value of the respective error sets.

Table 4: HPF positioning errors post calibration

	X [nm]	*Y* [nm]	*Z* [nm]	θx [μradian]	θy [μradian]	θz [μradian]
COMMAND DISPLACEMENT						
1 σ	14	34	26	0.5	0.4	0.2
Maximum	36	93	74	1.6	1.0	0.5
PARASITIC DISPLACEMENTS						
1 σ	40	50	321	2.2	1.7	0.7
Maximum	140	195	1032	7.4	8.8	2.5

The parasitic errors are clearly of more concern than the errors in commanded position. In particular, the parasitic errors in the *Z* axis are significantly larger than those in *X* and *Y*. The *Z* errors are larger as there is poor correlation between command values and some of the non-calibrated parasitic *Z* errors. This can be seen by inspecting the third row of the R matrix. Other parasitic errors (other rows) have several low $\boldsymbol{R_{ij}}$ values; however the magnitude of the errors for their good (near unity) $\boldsymbol{R_{ij}}$ values is lower than those for *Z* parasitic errors. A direct link between the hardware and the large magnitude/poor correlation of *Z* axis error has not been established. This relationship and other means of reducing parasitic errors are a main focus of continued work.

The non-calibrated model links a vector of actuator inputs, ***A***, to the model's position and orientation vector, $\boldsymbol{PO_M}$, via a transformation matrix, ***T***. The relationship is shown in Eqxn. 33.

$$PO_M = T \cdot A \tag{33}$$

$\boldsymbol{PO_M}$ is pre-multiplied by the calibration matrix to remove the linear systematic errors from the system. The resulting relationship, shown in Eqxn. 34, links the design parameters of the HPF to the calibrated performance of the HPF.

$$PO_C = C \cdot PO_M = C \cdot T \cdot A \tag{34}$$

The calibrated forward and reverse kinematics may then be calculated via normal matrix multiplication and inversion techniques. Equation 35 shows the solution for actuation inputs as a function of the calculated transformation matrix, the calibration and the desired position and orientation.

$$A = T^{-1} \cdot C^{-1} \cdot PO_C \tag{35}$$

The experimental calibration exercise (six tests) takes less than one hour and is therefore a less costly and time intensive way to achieve better performance in comparison to the setting of tight manufacturing and assembly tolerances. The experimental measurements and subsequent calculations may be automated, thereby making it possible for the HPF to be self calibrating over time.

6.4. Verification of no sliding condition

A test was run to determine if the flexures would prevent relative sliding and stick slip at the ball-groove contacts. For a preload of 225 N, the normal load, F_n, on each contact surface is 38-75 N. This corresponds to a tangential contact stiffness of 22 N/µm. The maximum tangential force that may be applied before slip occurs is given by $F_t = \mu F_n$, where μ is the static friction coefficient. For lubricated steel on steel, $\mu = 0.16$ and the corresponding tangential force, F_t, is 12 N. The maximum displacement that may be expected before siding occurs is 0.5µm. Before the test run, the HPF was engaged, preloaded to 225 N and then allowed to settle for 30 seconds. The HPF was then commanded to move in 4 nm increments through a range of 3 microns. The results in Fig. 22 do not show discontinuities in the plot. This proves that the groove flexures are successfully preventing relative sliding and stick-slip between the balls and grooves.

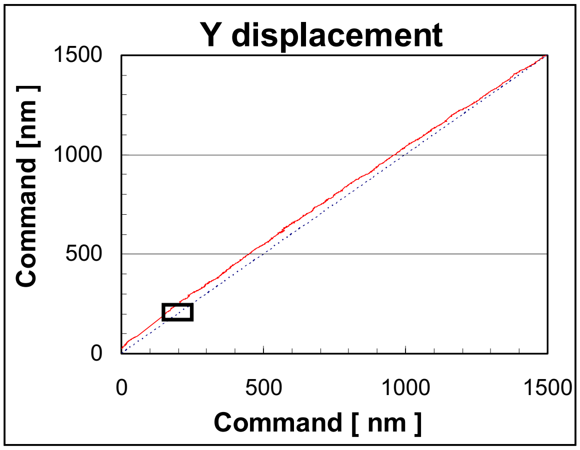

Figure 22: Displacement test results for coupling displacement while balls are engaged in grooves

Although smooth motion of the HPF may be assumed via use of the guiding and groove flexure bearings, it is helpful to validate this behavior and understand the smallest motion increment which may be achieved through the HPF. Figure 23 shows a magnified view of the rectangular detail in Fig. 22. The figure indicates that the engaged resolution of the HPF is approximately 4nm. This limit is due to limitations of the electronics that drive the piezo actuators.

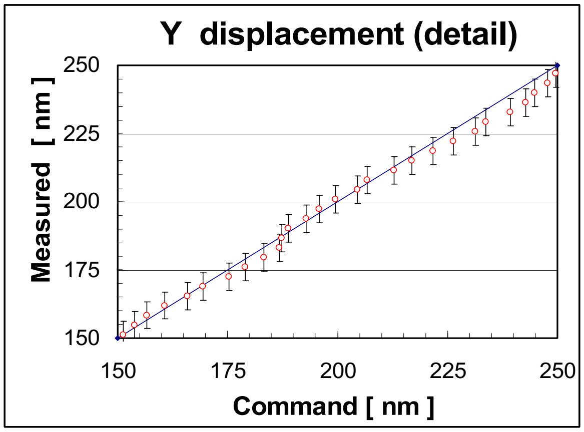

Figure 23: Close up of rectangular detail in Fig. 22

6.5. HPF repeatability in fixture mode

One thousand cycles of engagement and disengagement were performed over the course of the 14 hour repeatability test. The HPF was placed in fixture mode, meaning that the actuators were not used to enhance positioning performance. Positioning occurred solely due to the ball-grove interface interactions and groove flexure bearing motions. Ideally, the actuators would be commanded to hold their position throughout the test. Although the piezos are equipped with internal strain gage sensors which could be used to maintain the position to better than 5nm, the limitations of our dSpace system prevent us from simultaneously reading six capacitance probes, reading six strain gages and supplying independent voltages to the six piezos. A compromise approach was implemented in which the piezo actuators were energized with a constant voltage during the duration of the test. As such, the repeatability data will include errors from the piezo actuator creep. The results of the test are shown in Fig. 24.

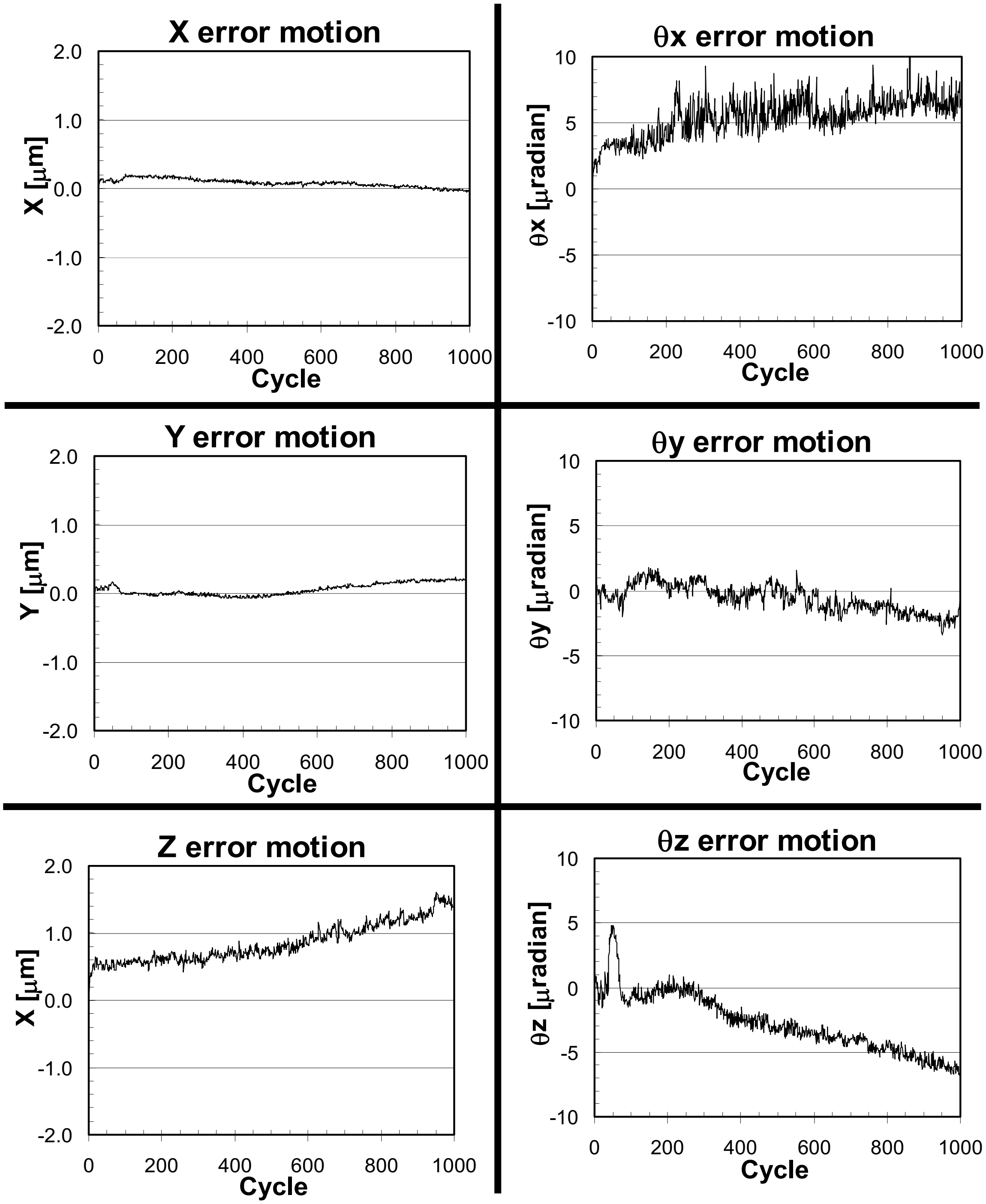

Figure 24: Repeatability tests with piezo actuators set at constant voltage

We may make several observations from the test results:

(1) Wear in and long-term stability: Due to the drift – this is clearly seen in the Z data – it is difficult to make any statements regarding the wear-in behavior of the fixture or the long-term stability. These errors are not a primary concern as they are known to be on the order of the surface finish [05] and therefore they may be easily corrected by periodic self-calibration and/or feedback control of the actuators.

(2) Random errors: Due to the drift min the piezos, the data should be considered in terms of short-term (point-to-point, PP) performance rather than the long-term (absolute, ABS) performance. Table 5 provides the one sigma repeatability in each of the six axes for PP and ABS.

Table 5: Fixture repeatability data (values correspond to 1 standard deviation)

	X [nm]		Y [nm]		Z [nm]		θx [μradians]		θy [μradians]		θz [μradians]	
Mates	ABS	PP	ABS	PP	ABS	PP	ABS	PP	ABS	PP	ABS	PP
0 - 100	36	14	53	12	68	39	0.60	0.28	0.60	0.28	2.00	0.43
700-1000	30	9	34	9	163	35	0.60	0.61	0.60	0.28	2.00	0.27
0 - 1000	58	11	87	11	288	38	1.4	0.65	1.00	0.29	2.30	0.32

The PP values indicate the fixture can be repeatable on the level of tens of nanometers and fractions of micro-radians if actuation inputs remain steady. This level of performance from a passive fixture is thought to be due to elimination of ball-groove stick slip. Stick slip prevents the balls from settling into their lowest energy state and therefore limits the repeatability of kinematic couplings [11]. As the balls settle into the grooves, the balls and grooves slide in the directions indicated by the exaggerated wear patterns in Fig. 8. The groove flexures prevent the random stick slip phenomena at the ball-groove contacts, thereby enabling the HPF to settle into a state which is closer to its minimum energy state. Although lubricants can be used to reduce this effect [12] when flexure bearings are not used, such an approach is limited to non-vacuum applications. We hypothesize that the flexures may also reduce the dependence of repeatability on the order of engagement of the balls and grooves. Both issues are subjects of continued work via experiments on kinematic couplings which are not equipped with actuators, but which are equipped with the same groove flexures.

6.6. Stiffness characteristics

The fixture was preloaded to provide approximately 7 N/micron stiffness in the x, y and z directions. The *X* and *Y* stiffness were obtained by hanging weights on the distal end of a string and attaching the proximal end to the fixture. The string was routed such that the tension in the string was directed parallel to the plane of coupling and through the coupling centroid. A comparison of predicted and experimental results is provided in Table 6. Experimental results show that the fixture is stiffer than expected by approximately 30 %. This was expected as the modeling approach assumed conservative values for the stiffness of individual compliant components. A better match between theory and measurement is desired; therefore future work will be focused upon improving the accuracy of the model.

Table 6: HPF stiffness – experimental vs. analytical results

	Kx [N/μm]	*Ky* [N/μm]	*Kz* [N/μm]
Experimental	10.0	10.0	10.1
Analytical model	7.1	7.1	7.3
% error	29.7	29.2	27.9

6.7. Dynamic characteristics

Although the dynamic characteristics of the HPF were not a primary focus of this work, tests were conducted to compare the behavior of the HPF with dynamic modeling tools which are under development. The tests were conducted with a preload of 225 N. Figure 25 shows the natural frequency at 200 Hz for a first mode of translation in the *z* directions. The majority of the groove-equipped component, e.g. the monolithic base, is physically grounded or directly adjacent to ground during the test, therefore the mass of the top (e.g. ball-equipped component) comprises the major mass which is free to vibrate. It is possible to reduce the mass of this component by 50%, thereby increasing the natural frequency up to 40% (280 Hz). If higher frequencies are desired, this can easily be accomplished by increasing the thickness of the guide flexures and increasing the stiffness of the ball-groove contacts.

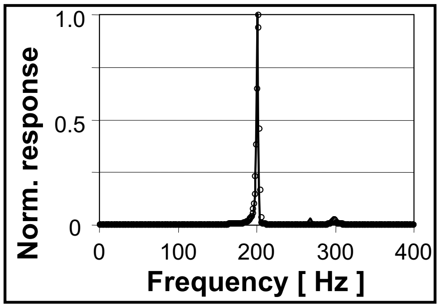

Figure 25: Normalized response of HPF dynamic characteristics

7. Summary

In this paper, we have introduced a hybrid positioning fixture which can be operated in two modes; as (1) a nanometer-level accurate and repeatable exact constraint fixture or (2) as a high load capacity, six-axis nanopositioner. Actuators, sensors and flexures are integrated into the structural loop of the fixture, thereby enabling controlled, changes in fixture geometry to add nanometer/micro-radian-level positioning capability. The integration of positioning and fixturing functions is made possible by:

(a) Ensuring that the flexure bearing's directions of high compliance are arranged parallel to the directions in which we wish to actuate. These directions are laid out so that they do not have a detrimental effect on the HPF stiffness when a high-stiffness actuator is used in parallel with the flexure.

(b) Ensuring that the flexure bearings' directions of high stiffness and high load capacity are aligned with the vectors of force transmittal through the fixture's structural loop, thereby enabling high load capacity and stiffness.

Models of fixture kinematics and fixture stiffness were generated and used to design a proof-of-concept, moving groove HPF prototype. When operated in fixture mode, experiments show standard deviation in point-to-point repeatability of 11, 11, and 40nm in x, y, and z; and 0.7, 0.3, and 0.3 micro-radians in θx, θy and θz. When operated in Nanopositioner mode, the device demonstrated 5nm resolution motion increment and range of 40x40x80 microns in translation and 800x800x400 micro-radians in rotation. The fixture possesses a load capacity of 450 N, a measured stiffness of 10 N/micron and natural frequency of 200 Hz.

8. Acknowledgements

This work was supported, in part, by the Ford Motor Company and the Ford-MIT alliance. The authors wish to thank the alliance and Ford Motor Company for their technical and financial support. This material is based in-part upon work supported by the National Science Foundation under Grant No.

0348242. The authors would also like to thank Mr. Gerry Wentworth and Mr. Mark Belanger for the efforts in fabricating the fixture prototype.

9. References

[01] Culpepper, M. L., M. K. Varadajan and M. Dibiaso, "Design of integrated eccentric mechanisms and exact constraint fixtures for micron-level repeatability and accuracy," Precision Engineering, 29 (1), 65 – 80, January 2005.

[02] Barraja, M. and Vallance, R. Tolerance Allocation for Kinematic Couplings, Proceedings of the 2002 ASPE Summer Conference, July 2002.

[03] Taylor, JB, and Tu, JF Precision X-Y Microstage with maneuverable kinematic coupling mechanism, Prec Eng, April, 1996, vol. 18, No. 2, p.85 – 94.

[04] Chui, MA, Roadmap of mechanical systems design for the semiconductor automatic test equipment industry, MIT Ph.D. thesis, 1998.

[05] Slocum A. Design of Three-Groove Kinematic Couplings. Prec Eng 1992;14;67-73.

[06] Hale, LC., Principles and techniques for designing precision machines, MIT Ph.D. Thesis, 1999, Cambridge, Ma.

[07] Schouten CH, Rosielle PCJN, Schellekens PHJ. Design of a kinematic coupling for precision applications. Prec Eng;20;46-52.

[08] Culpepper, M. L., "Design of Quasi-Kinematic Couplings," Precision Engineering, 28 (3), 338 – 357, July 2004.

Mangudi, K. and Culpepper, M. L., "Active, Compliant Fixtures for Nanomanufacturing," 2004 Annual Meeting of the American Society for Precision Engineering, Orlando, FL. October 2004, pp 113 – 116.

[09] Culpepper, M. L., A.H. Slocum and F. Z. Shaikh, "Compliant Kinematic Couplings for Use in Manufacturing and Assembly," Proceedings of the 1998 International Mechanical Engineering Congress and Exposition, Anaheim, CA, November 1998, pp 611 – 8.

[10] Mangudi, K. and Culpepper, M. L., "Active, Compliant Fixtures for Nanomanufacturing," 2004 Annual Meeting of the American Society for Precision Engineering, Orlando, FL. October 2004, pp 113 – 6.

[11] Hale LC, Slocum AH. Optimal Design Techniques for Kinematic Couplings. Prec Eng;25;114-27.

[12] Slocum AH, Donmez A. Kinematic couplings for precision fixturing- Part 2: Experimental determination of repeatability and stiffness. Prec Eng 1988;10;115-2.